



mDixon-based synthetic CT generation via transfer and patch learning

Xin Song^{a,b}, Pengjiang Qian^{a,b,*}, Jiamin Zheng^{a,b}, Yizhang Jiang^{a,b}, Kaijian Xia^c,
Bryan Traughber^{d,e}, Dongrui Wu^f, Raymond F. Muzic Jr^g

^a School of Artificial Intelligence and Computer Science, Jiangnan University, Wuxi 214122, China

^b Jiangsu Key Lab of Media Design and Software Technology, Jiangnan University, Wuxi 214122, China

^c Changshu Hospital Affiliated to Soochow University (Changshu No.1 People's Hospital), Changshu 215500, China

^d Case Center for Imaging Research and Department of Radiation Oncology, Case Western Reserve University, Cleveland, OH 44106, United States

^e Department of Radiation Oncology, University Hospitals Seidman Cancer Center and Department of Radiation Oncology, Louis Stokes Cleveland VA Medical Center, Cleveland, OH 44106, United States

^f Key Laboratory of the Ministry of Education for Image Processing and Intelligent Control, School of Automation, Huazhong University of Science and Technology, Wuhan 430074, China

^g Department of Radiology and Case Center for Imaging Research, University Hospitals, Case Western Reserve University, Cleveland, OH 44106, United States

ARTICLE INFO

Article history:

Received 4 February 2020

Revised 15 June 2020

Accepted 19 June 2020

Available online 21 June 2020

Keywords:

Synthetic CT

mDixon MR

Abdomen

Transfer learning

Patch learning

ABSTRACT

We propose a practicable method for generating synthetic CT images from modified Dixon (mDixon) MR data for the challenging body section of the abdomen and extending into the pelvis. Attenuation correction is necessary to make quantitatively accurate PET but is problematic with PET/MR scanning as MR data lack the information of photon attenuation. Multiple methods were proposed to generate synthetic CT from MR images. However, due to the challenge to distinguish bone and air in MR signals, most existing methods require advanced MR sequences that entail long acquisition time and have limited availability. To address this problem, we propose a voxel-oriented method for synthetic CT generation using both the transfer and patch learning (SCG-TPL). The overall framework of SCG-TPL includes three stages. Stage I extracts seven-dimensional texture features from mDixon MR images using the weighted convolutional sum; Stage II enlists the knowledge-leveraged transfer fuzzy c-means (KL-TFCM) clustering as well as the patch learning-oriented semi-supervised LapSVM classification to train multiple candidate four-tissue-type-identifiers (FTTIs); Stage III synthesizes CT for new patients' mDixon images using the candidate FTTIs and voting principle. The significance of our method is threefold: (1) As the global model for patch learning, guiding by the referenced knowledge, KL-TFCM can credibly initialize MR data with overcoming the individual diversity. As the local complement, LapSVM can adaptively model each patch with low time and labor costs. (2) Jointly using the transfer KL-TFCM clustering and patch learning-oriented LapSVM classification, SCG-TPL is able to output accurate synthetic CT in the abdomen. (3) SCG-TPL synthesizes CT only using easily-obtainable mDixon MR images, which greatly facilitates its clinical practicability. Experimental studies on ten subjects' mDixon MR data verified the superiority of our proposed method.

© 2020 Elsevier B.V. All rights reserved.

1. Introduction

Providing superior soft tissue contrast and high anatomical resolution, Magnetic Resonance (MR) images have been widely applied in clinical care and medical research [49,50]. Different from Computed Tomography (CT), MR does not use ionizing radiation which is particularly problematic for pediatric and pregnant patients. Positron Emission Tomography (PET) imaging is comple-

mentary to MR and is routinely used to image the ¹⁸F-labeled 2-fluoro-2-deoxy-D-glucose (FDG) distribution in cancer patients where focal uptake of FDG visualizes neoplasms [37]. Indeed, their combined value has motivated the creation of PET/MR scanners, which combines the both advantages of PET and MR in a single scanner. A challenge of this relatively new type of hybrid scanner is making the FDG PET images quantitatively accurate as the scanner lacks a CT which is the source of information for attenuation correction, the single largest correction of PET image reconstruction. Another high-value application of MR is for radiation treatment planning (RTP). The soft tissue contrast of MR usually provides much better visualization of the tumors to be targeted for

* Corresponding author at: School of Artificial Intelligence and Computer Science, Jiangnan University No. 1800 Lihu Avenue, Wuxi, Jiangsu, 214122, China.

E-mail address: qianpjiang@jiangnan.edu.cn (P. Qian).

treatment than does CT. However, as noted in the PET/MR discussion, MR lacks the photon attenuation information needed to calculate the tissue radiation dose. Whereas CT is traditionally used to provide this information, it would be ideal if it could be obtained directly from MR. This would obviate CT scanning which requires a different device and for which the patient position could be not exactly the same as during the MR scan. Further, obviating the CT scan could support an MR-only workflow which would enable patients to imaged and treated simultaneously using a linac-MR system [13]. This could achieve precise tumor targeting, taking into account not only tumor shrinkage over the multi-day time course of treatment but also taking into account changes in tumor position caused by physiologic (cardiac, respiratory) motion [16,44]. However, MR and PET/MR are rarely used individually in radiotherapy due to the lack of geometric integrity [41] and precision in mapping relative electron density (RED) [8] for dose calculations.

Both PET/MR and MR-only treatment are important advancements in medicine [31]. In both, the primary problem technical to be solved is the calculation of photon (gamma-or x-ray) radiation absorption by tissue. So the synthesis of CT from MR is a very attractive approach. The normal clinical processing can be used with the substitution of a synthetic CT (sCT) in place of a measured CT. To this end, multiple methods were proposed to generate synthetic CT from given MR images, such as the atlas-based [14,15], template-based [24], and voxel-based methods [40].

However, the diversity and real-time motion of human organs and tissues directly cause some methods to fail, particularly impacting some atlas-based and template-based methods [9,20]. In addition, two aspects of limitations on synthesizing CT images are worth being clarified as follows. One is from the perspective of body sections. Most studies have focused on the brain or pelvis (Andreasen et al., 2016; 12,19,27,28), and these body sections have the common characteristics of relatively simple organs that are relatively rigid. In contrast, the abdomen is a challenging body section, and because of its complex anatomical structure and the large amount of organ deformation caused by human respiration, this body section is rarely studied. The other concerns the MR sequences involved. To capture the bone signal during MR imaging, many existing methods made use of advanced sequences that require extra scanning time and are technically challenging for clinic applications, such as ultrashort echo time (UTE) [26] and zero echo time (ZTE) [7]. Not only does the abdomen contain vertebral bodies (large bones), the often the imaging field of view extends into the pelvis where there is the pelvic skeleton and top of the femurs.

In this context, our study attempts to present a novel, practicable voxel-based synthetic CT generation method that is qualified to effectively distinguish all of the tissue types in abdomen only in terms of commonly-available mDixon MR images. We refer to it as synthetic CT generation using both transfer [32,33] and patch learning (SCG-TPL for short) [46]. SCG-TPL involves three stages. The first is responsible for extracting effective texture features on given mDixon MR images. The second figures out multiple candidate four-tissue-type identifiers (FTTIs) by means of the knowledge-leveraged transfer fuzzy c-means (KL-TFCM) [34] clustering and the patch learning-oriented semi-supervised Laplacian support vector machine (LapSVM) [5] classification. The third stage synthesizes CT for new patients' MR images according to the multiple candidate FTTIs and the voting principle. The contributions of our study are mainly the following three points:

- (1) KL-TFCM is used as the global model for patch learning throughout our SCG-TPL method. Assisting by the referenced knowledge, KL-TFCM is capable of initializing the MR data with overcoming the individual diversity. LapSVM is enlisted to locally, precisely model each patch only with a small

quantity of manually-labeled tissue types. In this way, our method has low time and labor costs.

- (2) Jointly using the transfer fuzzy clustering and patch learning-oriented semi-supervised LapSVM classification, SCG-TPL is able to output desirable synthetic CT in the challenging abdomen and extending into the pelvis.
- (3) SCG-TPL synthesizes CT only using easily-obtainable mDixon MR images, which greatly facilitates its clinical practicability.

The rest of this manuscript is organized as follows. Related work, such as patch learning (PL), KL-TFCM, and LapSVM, are briefly introduced in Section 2. The proposed SCG-TPL method is introduced in detail in Section 3. Our experimental studies as well as result analyses are presented in Section 4. The conclusion is given in Section 5.

2. Related work

2.1. Patch learning (PL)

Patch learning [46] refers to a series of machine learning frameworks that jointly use one global model and multiple local models. PL supposes that most data work well with the global model. Exceptions compose the so-called patches in each of which the partial, affiliated data contribute much to the learning error of the global model.

PL proposes to model each patch adaptively. Generally, the local models are the complementary to the global one. As such, incorporating the power of both the global and patch-oriented local models, PL aims to achieve the overall high learning performance.

Fig. 1 depicts the PL procedure. Fig. 2 depicts the distribution of the dataset after applying global model. The rectangle presents the whole dataset. If the data fall into the global area, use the global model. If the data fall into any patch, use the corresponding patch model. Thus, we can determine which model should be used in the whole procedure of patch learning. Specifically, PL consists of the following four steps:

1. Obtain a global model using all of the training data;
2. Identify the data parts that present poor performance in the global model as patches;

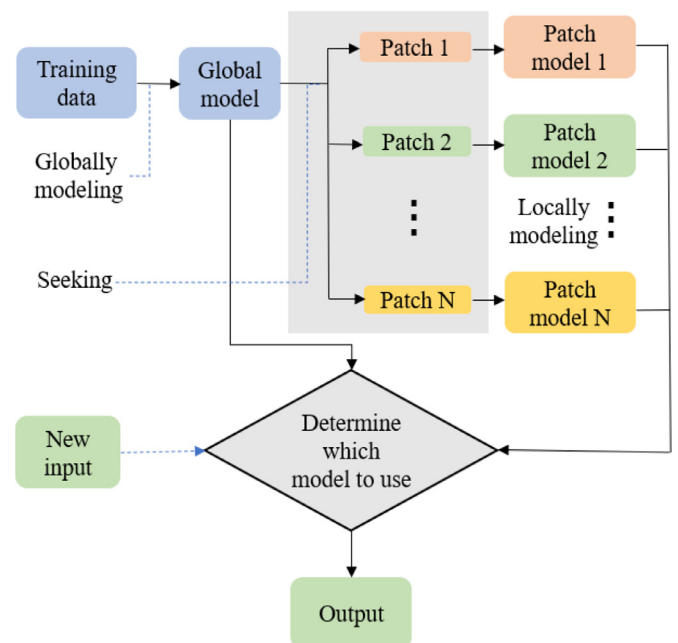


Fig. 1. The procedure illustration of PL.

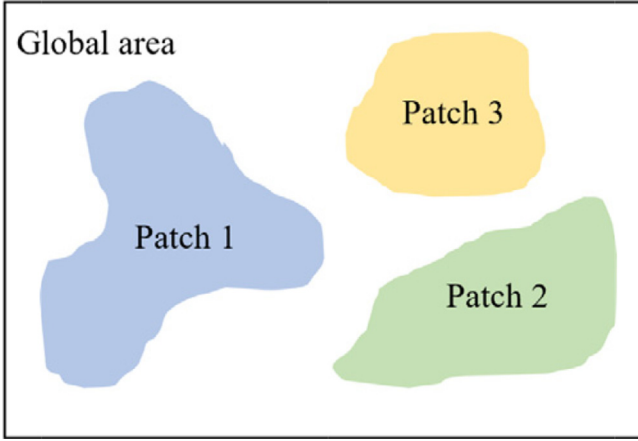


Fig. 2. The data distribution after applying the global model.

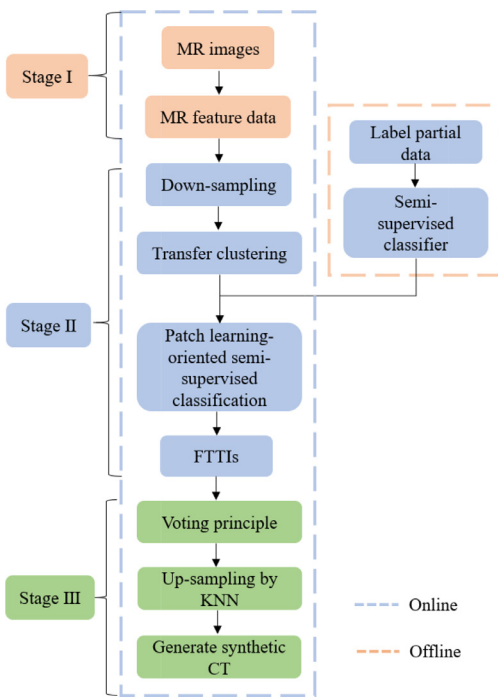


Fig. 3. Illustration of work and data flows of SCG-TPL.

3. Determine the locally adaptive model for each patch;
4. Handle new data: 1) using the global model if the data do not belong to any patch; 2) using the adaptive local model if the data fall into the corresponding patch.

2.2. KL-TFCM

As is well-known, the effectiveness of fuzzy c-means (FCM) [4,35,45] is often significantly impacted by noise and outliers contained in target data sets. To address this issue, we integrated the transfer learning [21,52] into the framework of classical fuzzy c-means (FCM) and proposed the KL-TFCM algorithm.

Let $X_T = \{\mathbf{x}_{1,T}, \dots, \mathbf{x}_{N_T,T}\} \in \mathbb{R}^{N_T \times d}$ denote the data set in the target domain, where the example number is denoted as N_T and the data dimension is denoted as d . Let $\mathbf{U}_T = [\mu_{ij,T}]_{C_T \times N_T}$ denotes the $C_T \times N_T$ membership matrix in the target domain, with $\mu_{ij,T}$ signifying the membership degree of $x_j (j = 1, \dots, N_T)$ belonging to cluster $i (i = 1, \dots, C_T)$, where the cluster number is denoted by C_T . $\mathbf{V}_T = [v_{1,T}, \dots, v_{C_T,T}]^T$ denotes the cluster prototype matrix in the

target domain, with $v_{j,T} = [v_{j1,T}, \dots, v_{jd,T}]^T (j = 1, \dots, C_T)$ signifying the j^{th} cluster prototype (centroid). $\tilde{\mathbf{V}}_S = [\tilde{v}_{1,S}, \dots, \tilde{v}_{C_T,S}]^T$ denotes the employed cluster representatives from the source domain for the eventual knowledge utilization in the target domain, with $\tilde{v}_{j,S} = [\tilde{v}_{j1,S}, \dots, \tilde{v}_{jd,S}]^T (j = 1, \dots, C_T)$ denoting the j^{th} cluster representative in the source domain.

Here we would like to clarify that $\tilde{\mathbf{V}}_S$ can be the historical cluster prototypes (also called cluster centroids) \mathbf{V}_S of the source domain if and only if the cluster numbers of the target and source domains are the same. What needs to be further explained is that both cluster prototypes and cluster representatives represent the cluster centroids of the source domain during transfer learning. Due to the existence of the case where the cluster numbers in the source and target domains are inconsistent, only part of the cluster centroids in the source domain are utilized as the prior knowledge for the transfer learning in the target domain. These partially involved cluster centroids of the source domain are called as the cluster representatives in our study.

The framework of KT-TFCM can be reformulated as

$$\min \left(\begin{aligned} & J_{\text{KT-TFCM}}(\mathbf{U}_T, \mathbf{V}_T) = \\ & \sum_{i=1}^{N_T} \sum_{j=1}^{C_T} \mu_{ij,T}^m \|\mathbf{x}_{i,T} - v_{j,T}\|^2 \\ & + \lambda \sum_{j=1}^{C_T} \|\mathbf{v}_{j,T} - \tilde{v}_{j,S}\|^2 \end{aligned} \right) \quad (1)$$

s.t. $i \in [1, N_T], j \in [1, C_T]$,

$$\mu_{ij,T} \in [0, 1], \sum_{j=1}^{C_T} \mu_{ij,T} = 1$$

where $\mathbf{x}_{i,T} (i = 1, \dots, N_T) \in X_T$, $v_{j,T} \in V_T$, $\tilde{v}_{j,S} \in \tilde{\mathbf{V}}_S$, and $\lambda \geq 0$ is a regularization coefficient. Parameter λ is the impact factor and determines the learning degree between the target and source domains. Eq. (1) is a minimization problem, thus larger values of λ indicate that the target domain learn much from the source domain, i.e., V_T is V_S .

The update of the cluster centroid $v_{j,T}$ and fuzzy membership $\mu_{ij,T}$ can be deduced using the Lagrange optimization as follows

$$v_{j,T} = \frac{\sum_{i=1}^{N_T} \mu_{ij,T}^m \mathbf{x}_{i,T} + \lambda \tilde{v}_{j,S}}{\sum_{i=1}^{N_T} \mu_{ij,T}^m + \lambda} \quad (2)$$

$$\mu_{ij,T} = \frac{1}{\sum_{i=1}^{C_T} \left(\frac{\|\mathbf{x}_{i,T} - v_{j,T}\|^2}{\|\mathbf{x}_{i,T} - v_{i,T}\|^2} \right)^{\frac{1}{m-1}}} \quad (3)$$

2.3. Laplacian support vector machine (LapSVM)

LapSVM [5,48], an extension of the traditional SVM, is a semi-supervised classification algorithm based on the manifold regularization [30], studies how to use a small number of labeled samples as well as numerous unlabeled samples to train classifiers, which is an extension of the traditional SVM. LapSVM leverages the intrinsic geometry information of samples because of the introduction of the manifold regularization term.

Assume $S = \{\mathbf{x}_i, i = 1, \dots, n\}$ denotes a sample set, \mathbf{x}_i represents the i^{th} sample and n represents the number of samples. Suppose that $L = \{\mathbf{x}_i, i = 1, \dots, m\}$ represents the labeled samples, where m represents the number of labeled samples; $U = \{\mathbf{x}_i, i = 1, \dots, u\}$ represents the unlabeled samples, where u represents the number of unlabeled samples. Let y_i represent the category of the i^{th} sample, $y_i \in \{-1, 1\}$. Then, the LapSVM framework can be represented

as

$$f^* = \min_{f \in H_k} \sum_{i=1}^m \max(1 - y_i f(\mathbf{x}_i), 0)_\pm + \gamma_A \|f\|_A^2 + \gamma_l \|f\|_l^2 \quad (4)$$

where $\mathbf{f} = [f(\mathbf{x}_i), \mathbf{x}_i \in S]^T$ is an n -dimensional column vector in the training dataset. $\|\cdot\|_A^2$ is the ambient norm defined in the regenerative nuclear Hilbert space (RKHS), and H_k is the RKHS related to the kernel function. Parameter γ_A controls the complexity of $\|f\|_A^2$ in RKHS. $\|f\|_l^2$ is the regularization term maintaining the inner manifold structure of the sample distribution. Parameter γ_l is the weight of the function in the low-dimensional manifold, which controls the complexity of the inner geometry function. By calculating the Lagrange multiplier, we obtain the classifier as follows.

$$f^* = \sum_{i=1}^n \alpha_i^* \mathbf{K}(\mathbf{x}_i, \mathbf{x}) \quad (5)$$

where α_i^* is the Lagrange multiplier and \mathbf{K} is the kernel matrix. Solving the Lagrange multiplier yields

$$\alpha^* = (2\gamma_A \mathbf{I} + 2\gamma_l \mathbf{K} \mathbf{L})^{-1} \mathbf{J}_L^T \mathbf{Y} \beta^* \quad (6)$$

where \mathbf{I} is the identity matrix and \mathbf{L} is the Laplacian matrix. $\mathbf{Y} \in \mathbb{R}^{m \times m}$ is a diagonal matrix composed of identification samples $\mathbf{y}_i, i = 1, \dots, m$. $\mathbf{J}_L \in \mathbb{R}^{m \times n}$ is a block matrix $[\mathbf{I} \mathbf{O}]$ formed by labeled samples and unlabeled samples. β is also the Lagrange multiplier:

$$\begin{aligned} \beta^* &= \max_{\beta \in \mathbb{R}^m} \sum \beta^i - \frac{1}{2} \beta^T \mathbf{Q} \beta \\ \mathbf{Q} &= \mathbf{Y} \mathbf{J}_L \mathbf{K} (2\gamma_A + 2\gamma_l \mathbf{K} \mathbf{L})^{-1} \mathbf{J}_L^T \mathbf{Y} \\ \text{s.t. } &\sum_{i=1}^m \beta_i y_i = 0, \\ &0 \leq \beta_i \leq 1, i = 1, \dots, m \end{aligned} \quad (7)$$

3. The proposed SCG-TPL method

The proposed SCG-TPL method overall includes three stages, as shown in Fig. 3. The first is the MR image data preparation stage to extract seven-dimensional features from given MR images. The second conducts transfer clustering as well as patch learning-oriented semi-classification to establish several candidate four-tissue-type-identifiers (FTTIs) via given training subjects. The last generates synthetic CTs for new patients according to the candidate FTTIs and voting principle. Next, we describe each stage in detail.

3.1. MR image data preparation

Feature extraction is of vital importance to our proposed SCG-TPL method. Considering the potential uncertainty (e.g., environmental noise and organ motion) during acquiring MR images, we adopt the strategy of weighted convolutional sum to extract local texture features from the MR images. As we previously introduced in [11], four different types of MR images: fat, water, in-phase (IP) and opposed-phase (OP) were available for each subject. Thus, similar to what we did in [51], we first concurrently extract the texture features using the weighted convolutional sum from the four MR images of each subject. Then, the spatial information of voxels is also included in our current study to further augment the voxel features. One can refer to [51] for the details. As such, eventually, we can constitute the seven-dimensional MR feature data for the matching MR volume of each subject.

In addition, to overcome the individual diversity when handling different subjects' data, our method needs the referenced, prior knowledge, i.e., referenced class prototypes of bone, air, fat tissue

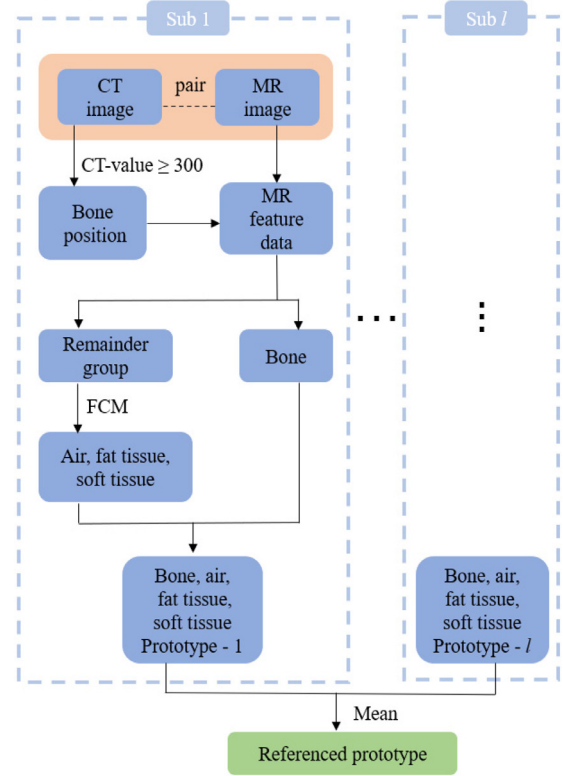


Fig. 4. Illustration of generation of the prior referenced cluster centroids.

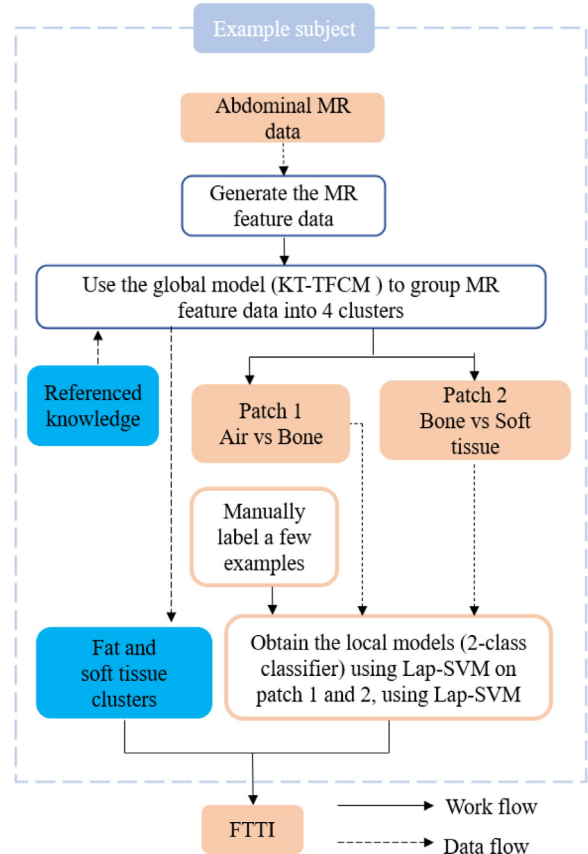


Fig. 5. Illustration of the work and data flows for generating the FTTI with an example subject.

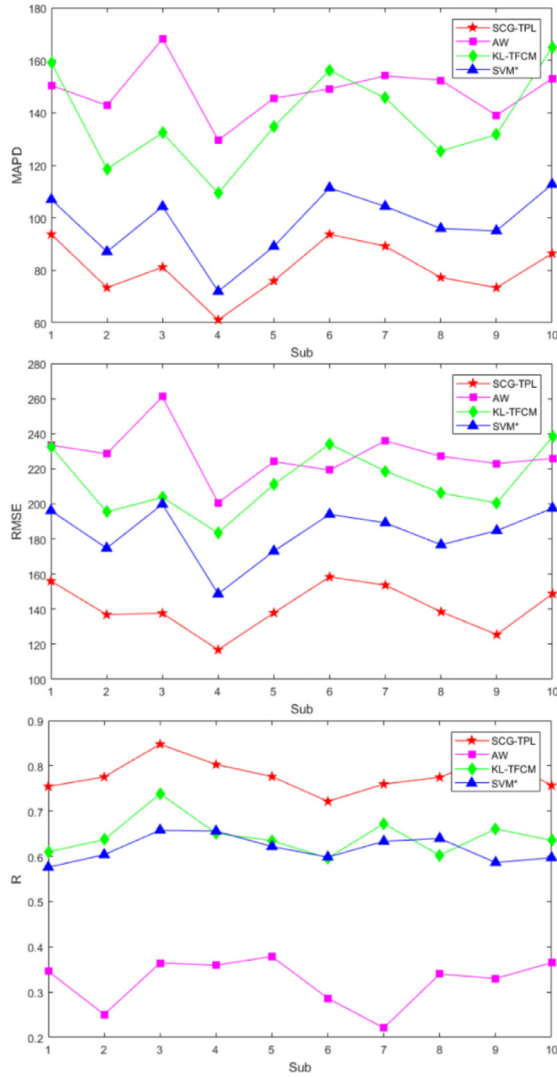


Fig. 6. Performance curves of the four methods.

and soft tissue, to assist the KL-TFCM clustering on target datasets. To this end, several historical patients' pairwise, registered CT-MR images are necessary. Suppose there are l historical patients available, the process for generating the prior knowledge can be sketched in Fig. 4. Specifically, on each historical patient's CT image, we obtain the positions of all bone tissue with the Hounsfield Unit (HU) value ≥ 300 . Then, mapping these obtained bone positions into the patient's MR images (IP, OP, fat, and water images), we consequently get the positions of all leftover tissues, i.e., fat, air, and soft tissue. On the seven-dimensional MR feature data of these positions, we run the classical FCM algorithm to get the three cluster centroids (namely, cluster prototypes). Here, depending on some clinical experience and referenced values from existing literature [38], we know the correspondence between cluster centroids and tissue types with regard to air, fat, and soft tissue, respectively [1,3,17,18,23,42]. To embody the overall properties over different patients, the average values of the l calculated cluster centroids regarding bone, air, fat, and soft tissue are enlisted as the final referenced knowledge for transfer learning in KL-TFCM.

3.2. Constructing candidate four-tissue-type-identifiers (FTTIs)

Our objective is to generate accurate synthetic CT from given MR images in the challenging abdomen body section and extend-



Fig. 7. The histograms of metrics for all methods.

ing into the pelvis. In [36] we proposed to use a systematic, five-phase-interlinked method to achieve this goal. Inspired by patch learning, here we attempt to put forward a simplified approach. To this end, several subjects' mDixon MR images are needed to get several candidate FTTIs. Let's suppose m training subjects are available in this stage. In our designed SCG-TPL method, KL-TFCM is employed as the global model to implement patch learning. That is, KL-TFCM is capable of measuring which partitions of data have satisfactory clustering effectiveness and which should be treated as the patches that need to be individually optimized using the corresponding local models.

Taking one subject as the example, we explain our process. On one subject's MR feature data, after running KL-TFCM, we find that only the obtained fat and soft tissue groups are generally satisfactory, but not the others, due to the fact that mDixon sequences are proficient in exhibiting fat and soft tissues. Particularly, we found that voxels between air and bone cannot be incorrectly grouped by KL-TFCM [6,29], and similar situations happen on quite a few voxels between bone and soft tissue (e.g., cartilage looks like soft tissue). This means that "bone VS air" and "bone VS soft tissue" should be regarded as two patches in our study.

Consequently, LapSVM is enlisted as the locally modeling method in our design as it can figure out insightful classifiers with a very small quantity of labeled examples. Therefore, for the patch

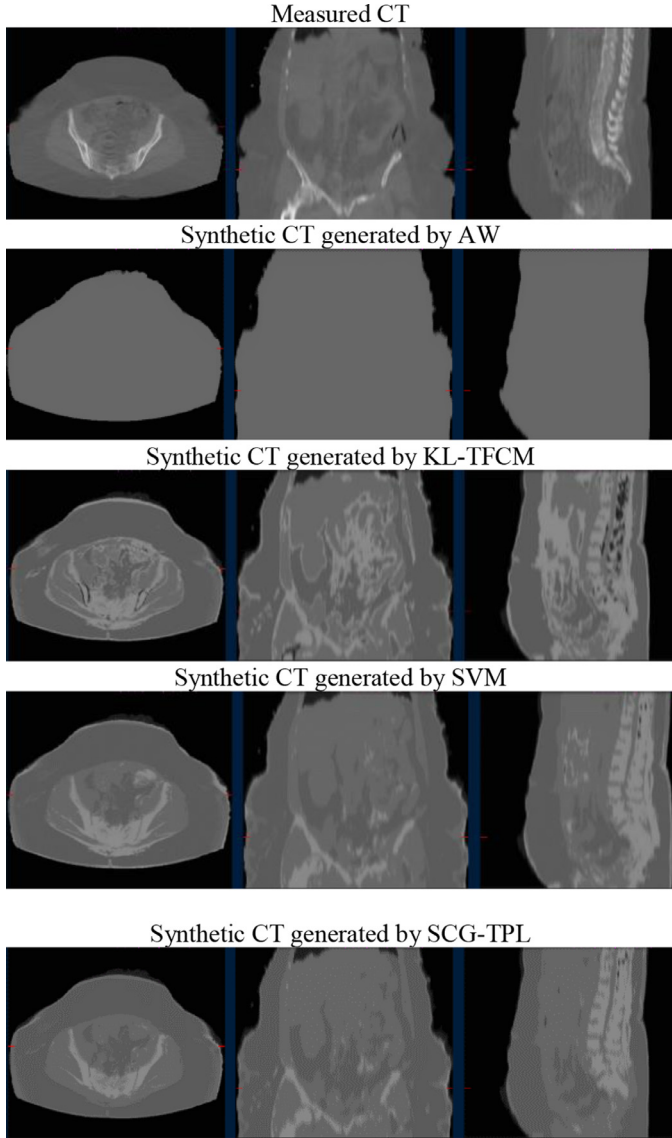


Fig. 8. Synthetic CT images of a representative subject (Sub 8) using four methods.

of “bone VS air”, with manually labeling a few bone and air examples and using LapSVM, we are able to establish the two-class classifier to reliably distinguish the bone and air; likewise, for the patch of “bone VS soft tissue”, we train the two-class classifier to differentiate the bone and soft tissue.

So far, in summary, for this subject’s MR feature data, we first know voxels belonging to the fat and soft tissue by means of the global KL-TFCM model, and then in terms of the two local patch models, we can obtain the precise air and bone tissues as well as some remaining soft tissue that was initially, mistakenly grouped into bone. As such, we figure successfully out the FTI for this subject. Fig. 5 intuitively depicts this procedure.

On all of the m training subjects, we can achieve m FTIs. These are the base of our SCG-TPL method. Via them, and using the voting strategy, we are able to reliably predict the tissue types of voxels in new patients’ MR images.

Considering the large amount of MR data even in one patch, it is infeasible to directly take the entire data as the input to the local model, because the time consumption is considerable. Thus, we advise the “sampling + K-nearest neighbors (KNN)” mechanism to accelerate the process, i.e., randomly sampling the entire data for analysis in the beginning and using KNN to propagate the analysis results of the sampled subset to the whole data in the end.

Suppose the sampling size is denoted by ss and the choice of the nearest neighbors is denoted by k . As we have two patch models, we use $ss-1$ and $k-1$ to signify the parameters associated with Model 1 and $ss-2$ and $k-2$ with Model 2.

3.3. Generating synthetic CT images through multiple FTIs

We organically assemble the identification results of multiple FTIs via the strategy of voting to decide the tissue types of voxels in new patients’ MR data. Then, with assigning appropriate CT values to corresponding tissue types, we can synthesize the CT image for the given MR images. In our study, the CT values of bone, air, fat, and soft tissue are set to 380, -700 , -98 , and 32, respectively [38].

4. Experimental results

4.1. Setup

In this section, we assess the effectiveness of the proposed SCG-TPL method for generating synthetic CT images. Ten subjects were recruited using a protocol approved by the University Hospitals Cleveland Medical Center Institutional Review Board. To obtain pairs of aligned MR and CT images, OpenREGGUI, an open-source

Table 1
Parameters involved in SCG-TPL.

Parameters	Suggested settings	Trial ranges
Regularization parameter λ in KL-TFCM in (1)	$\lambda = 500$	$\lambda \in \{100, 200, 300, 400, 500, 600, 700, 800, 900, 1000\}$
Regularization parameter γ_A, γ_I in LapSVM in (4)	Determined by 10-fold cross-validation	$\gamma_A \in \{1e-8, 1e-6, 1e-4, 1e-2, 1e0, 1e1, 1e2, 1e3\}$ $\gamma_I \in \{1e-8, 1e-6, 1e-4, 1e-2, 1e0, 1e1, 1e2, 1e3\}$
N_l and N_u denote the data sizes of the labeled data and unlabeled data in the two patch models of SCG-TPL, respectively. N_l can be divided into N_{l-1} and N_{l-2} , representing the labeled data sizes in patch model-1 and patch-model-2, respectively, and similarly with N_u-1 and N_u-2 .	$N_{l-1} = 400$ $N_{l-2} = 1600$ $N_{u-1} = 400$ $N_{u-2} = 1600$	$N_l \in \{100, 200, 300, 400, 500, 600\}$ $N_u \in \{1900, 1800, 1700, 1600, 1500, 1400\}$
Parameter ss is the sampling data size in the patches. Parameter k is to select k nearest neighbors in KNN. Similarly, ss consists of $ss-1$ and $ss-2$, and k consists of $k-1$ and $k-2$.	$ss-1 = 3e4$ $k-1 = 3$ $ss-2 = 3e4$ $k-2 = 7$	$ss \in \{1e4, 2e4, 3e4, 4e4, 5e4, 6e4\}$ $k \in \{1, 3, 5, 7, 9\}$

Table 2

Performance comparison of synthetic CT image generation by the proposed SCG-TPL and other methods.

Sub		MAPD				RMSE				R			
		SCG-TPL	AW	KL-TFCM	SVM*	SCG-TPL	AW	KL-TFCM	SVM*	SCG-TPL	AW	KL-TFCM	SVM*
1	Mean	93.44	150.45	159.03	106.99	155.50	233.49	232.66	196.11	0.75	0.35	0.61	0.58
	Std.	0.10	0.00	1.02E-02	0.91	0.12	0.00	1.06E-02	0.76	3.50E-04	0.00	7.39E-06	1.00E-04
2	Mean	73.47	142.80	118.61	87.09	136.97	228.49	195.37	174.73	0.78	0.25	0.64	0.60
	Std.	0.05	0.00	1.01E-02	0.12	0.07	0.00	1.44E-02	0.05	2.31E-04	0.00	2.83E-05	1.33E-03
3	Mean	81.12	168.21	132.40	104.29	137.54	261.03	203.73	199.81	0.85	0.36	0.74	0.66
	Std.	0.08	0.00	1.04E-02	0.56	0.13	0.00	1.29E-02	0.09	2.93E-04	0.00	1.83E-05	2.55E-03
4	Mean	61.09	129.55	109.33	71.95	116.68	200.63	183.42	148.70	0.80	0.36	0.65	0.66
	Std.	0.05	0.00	6.71E-03	0.15	0.10	0.00	8.93E-03	0.08	4.72E-04	0.00	1.89E-05	1.50E-03
5	Mean	76.11	145.55	134.66	89.11	137.97	224.10	211.00	173.06	0.78	0.38	0.63	0.62
	Std.	0.09	0.00	2.15E-02	0.44	0.15	0.00	2.84E-02	0.19	3.99E-04	0.00	6.28E-05	1.78E-03
6	Mean	93.38	149.09	156.06	111.41	157.72	219.24	234.04	194.02	0.72	0.29	0.60	0.60
	Std.	0.15	0.00	8.54E-03	1.17	0.23	0.00	9.09E-03	1.05	5.55E-04	0.00	4.99E-06	3.76E-04
7	Mean	89.14	154.07	145.65	104.36	153.37	235.96	218.67	189.16	0.76	0.22	0.67	0.63
	Std.	0.14	0.00	1.73E-02	1.16	0.19	0.00	1.87E-02	0.98	3.86E-04	0.00	1.70E-05	6.50E-04
8	Mean	77.69	152.41	125.46	95.92	138.86	227.09	206.18	176.67	0.77	0.34	0.60	0.64
	Std.	0.10	0.00	9.63E-03	0.83	0.17	0.00	9.23E-03	0.60	3.68E-04	0.00	6.89E-06	3.06E-04
9	Mean	73.41	139.04	131.68	95.06	125.36	222.99	200.55	184.73	0.82	0.33	0.66	0.59
	Std.	0.07	0.00	6.74E-03	0.43	0.13	0.00	6.96E-03	0.19	4.26E-04	0.00	9.54E-06	3.37E-03
10	Mean	86.48	153.00	165.00	112.76	148.43	225.90	238.20	197.52	0.76	0.37	0.64	0.60
	Std.	0.13	0.00	1.18E-02	1.08	0.19	0.00	1.33E-02	0.74	6.45E-04	0.00	1.30E-05	1.89E-03
Average	Mean	80.53	148.42	137.79	97.89	140.84	227.89	212.38	183.45	0.78	0.32	0.64	0.62
	Std.	10.26	10.27	18.24	12.69	13.23	15.11	18.17	15.67	0.04	0.05	0.04	0.03
p-value		1.34E-09	5.74E-12	1.88E-09	1.56E-09	8.90E-11	3.93E-12	3.84E-11	3.79E-11	1.71E-13	1.30E-08	2.98E-12	1.74E-13

image registration package [22], was used in our study to perform the deformable registration. Therefore, we have ten sets of registered MR and CT images of the abdomen for study and we name them as Sub1 to Sub10.

Three existing methods were compared with our method, i.e., the all-water method (AW) [2], KL-TFCM and SVM*. In the AW method, all the voxels within the body are directly viewed as water, which is considered a common approximation in radiation treatment. KL-TFCM applies historical cluster centroids to assist clustering target MR feature data and the achieved 4 clusters are directly regarded as the types of voxels of the abdomen. SVM* denotes the alternative method in which the supervised SVM, i.e., the conventional SVM [39], is used to construct the patch model in comparison with LapSVM recruited in our method. This implies that SVM* utilizes only a few labeled examples to train the patch model without using any unlabeled data.

Furthermore, to fairly evaluate the effectiveness of involved methods, three common metrics—mean absolute prediction deviation (MAPD), root mean square error (RMSE), and R [10,43]—were used throughout our experiments.

The proposed SCG-TPL involves several parameters, as listed in Table 1. To optimize the effect of these parameters, we used the grid search [25] and 10-fold cross-validation [47] to ultimately assign appropriate values to each parameter.

It is worth clarifying that we adopted the leave-one-out strategy to generate synthetic CT image for each of the subjects. That is, we treat one subject as the new patient (the test subject) and the other leftover as the training subjects. Each result of generating the synthetic CT image of the new patient was assembled from the results of the nine remaining subjects' FTTIs, which excludes the one of the test subject itself.

Our experimental studies were carried out using a computer with an Intel i5-4570 3.20 GHz CPU, and 8 GB of RAM running Microsoft Windows 10 (64 bit), and MATLAB 2017a.

4.2. Results

We separately executed the SCG-TPL, AW, KL-TFCM, and SVM* methods on the MR feature data from the ten subjects. Each experiment was repeated 20 times. As listed in Table 2, the means and

standard deviations of validity metrics are calculated on each subject regarding these methods, and the average of the means and standard deviations are also reported. To indicate the performance of synthetic generation intuitively, the curves of the MAPD, RMSE and R metrics to ten subjects are shown in Fig. 6 and the histograms are further supplemented in Fig. 7 to intuitively demonstrate these performance comparisons. In Fig. 8, we display the synthetic CT images of the four methods on Subject 8.

Then, we evaluated the robustness of SCG-TPL against core system parameters. We analyzed the two parameters: ss and k . As previously mentioned, due to the existing two patch models, we subdivided ss and k into $ss1$, $ss2$, $k1$, and $k2$ for different patch models, i.e., $ss1$ and $k1$ for Patch 1 and $ss2$ and $k2$ for Patch 2. We first assigned the suggested values to these parameters and then on each patch and towards each subject we gradually changed one of the two parameters' values with keeping the other fixed. Meanwhile, the validity metrics, MAPD, RMSE and R, were recalculated accordingly. Fig. 9 shows the parameter robustness curves of the SCG-TPL method.

4.3. Experimental analysis and discussion

In Fig. 6, the performance curves show the trends of metric value changes between different subjects. Obviously, the proposed SCG-TPL method has lower values of mean absolute prediction deviation (MAPD), lower values of root mean square error (RMSE), and higher correlation (R) values than the other three methods: AW, KL-TFCM and the SVM*. Therefore, our SCG-TPL method has more satisfactory performance of synthetic CT generation.

In Fig. 7, we utilize the histograms to demonstrate the results of the four involved methods more visually. In the histograms, the heights indicate the mean values and the error bars show the standard deviations. All of the results of three metrics show that our proposed SCG-TPL method appears the best performance as well as comparable stability against the other three.

Results shown above indicate that our study successfully solves the challenging problem of synthetic CT generation on abdomen-pelvis with commonly-available mDixon MR images. Our SCG-TPL makes great improvements compared to the three existing methods according to the experimental results, both in terms of the

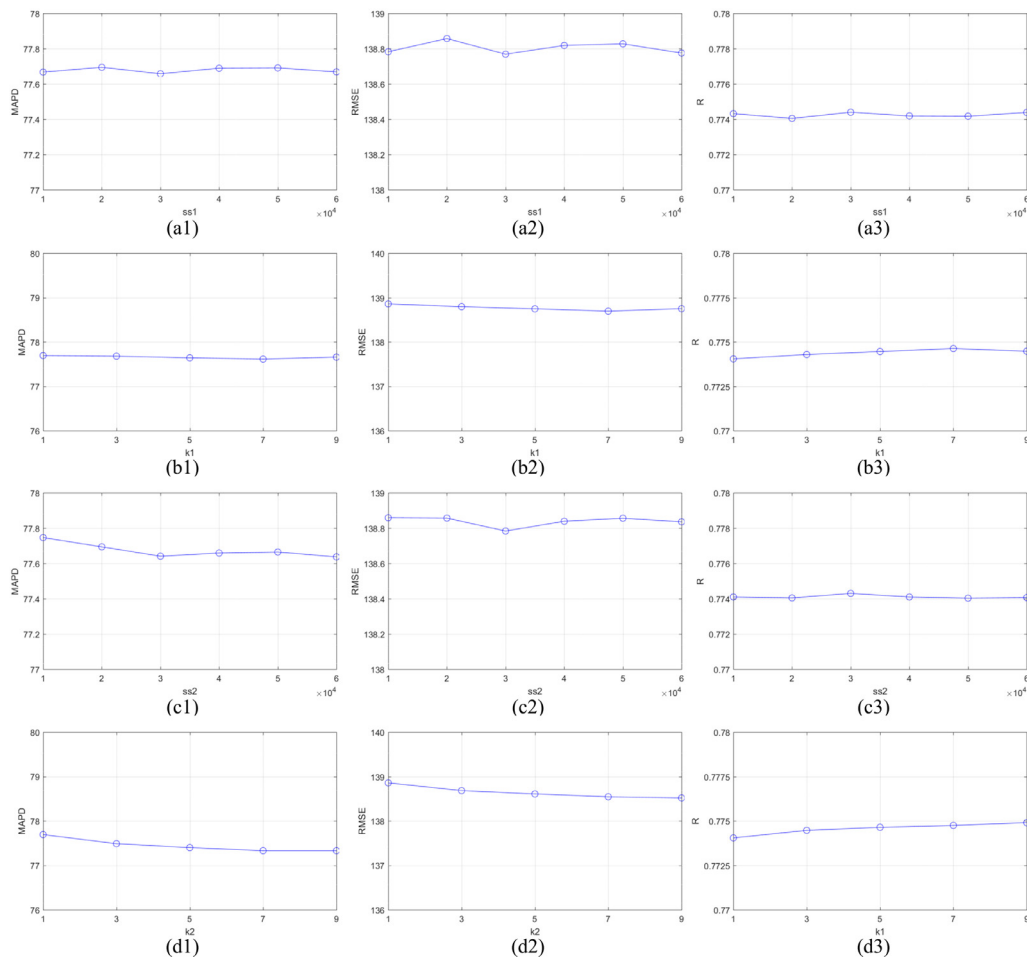


Fig. 9. Parameter robustness of the SCG-TPL method. (a1)–(a3) ss_1 vs. MAPD, RMSE and R. (b1)–(b3) k_1 vs. MAPD, RMSE and R. (c1)–(c3) ss_2 vs. MAPD, RMSE, R. (d1)–(d3) k_2 vs. MAPD, RMSE, R.

validity metrics and the generated synthetic CT images. As listed in Table 2, the proposed SCG-TPL method generally appears lower MAPD and RMSE values as well as higher R scores than the other three methods, including AW, KL-TFCM and SVM*. The average value of the MAPD of our proposed SCG-TPL is 80.53 ± 10.26 , which is significantly better than the 148.42 ± 10.27 result of AW, the 137.78 ± 18.22 result of KL-TFCM and the 97.89 ± 12.69 result of SVM*. Furthermore, we calculated p-values by a paired two-tailed t-test and $\alpha = 0.05$. The p-values are far less than 0.05, which also supports the significance of the improvement of our method.

Our proposed SCG-TPL also greatly improves the quality of the synthetic CT images. From Fig. 8, it is distinct that the synthetic CT image generated by KL-TFCM mixes large amounts of soft tissue and bone as well as a few areas of air and bone. The image quality generated by SVM* is slightly higher than that of KL-TFCM, because the mixing of air and bone is reduced, but the edges of soft tissue are still mixed with bone. Obviously, the synthetic CT generated by our SCG-TPL largely improves the quality and shows relatively clear and clean edges for each tissue type.

In SCG-TPL, KL-TFCM is used as the global model for patch learning. Assisted by the referenced knowledge, KL-TFCM is capable of effectively initializing the MR data with overcoming the individual diversity. Different from SVM* in which the traditional SVM is used to model patches, we recruit LapSVM to locally, precisely model each patch only with a small quantity of manually labeled examples, which greatly saves us time and labor-consuming, without any performance degradation. As such, jointly

using the KL-TFCM clustering and patch learning-oriented LapSVM semi-supervised classification, our SCG-TPL can output desirable synthetic CT in the challenging abdomen.

Last, as shown in Fig. 9 the fluctuation range of MAPD values is within 0.2% when ss_1 and ss_2 vary in the reasonable trial ranges. Similarly, the fluctuation range of MAPD is within 1% when k_1 and k_2 change in the trial ranges. These prove good parameter robustness of our method.

5. Conclusion

We study the complex abdominal body section in medical imaging to generate synthetic CT images with mDixon MR images only. Patching learning incorporating transfer learning is used, and the SCG-TPL method is proposed and evaluated. KL-TFCM is used to act as the global model during SCG-TPL works which, guided by the historical knowledge, is capable of stably, macroscopically grouping the MR image data into several tissue clusters and thereby recognizing the patches. Then, LapSVM, employing a few manually labeled examples as well as many unlabeled data, is enlisted to establish the local model matching each patch to complement the global model. In this way, our proposed SCG-TPL method creates accurate abdominal synthetic CT generation via easily-obtainable mDixon MR images only.

Declaration of Competing Interest

We declare that there is no conflict of interest.

References

- [1] D. Andreassen, K. Van Leemput, R.H. Hansen, J.A. Andersen, J. Edmund, Patch-based generation of a pseudo CT from conventional MRI sequences for MRI-only radiotherapy of the brain, *Med. Phys.* 42 (4) (2015) 1596–1605.
- [2] D. Andreassen, J.M. Edmund, V. Zografos, Computed tomography synthesis from magnetic resonance images in the pelvis using multiple random forests and auto-context features, in: *Medical imaging: Image processing*, 9784, International Society for Optics and Photonics, 2016.
- [3] D. Andreassen, K. Van Leemput, J. Edmund, A patch-based pseudo-CT approach for MRI-only radiotherapy in the pelvis, *Med. Phys.* 43 (8) (2016) 4742–4752.
- [4] J.C. Bezdek, R. Ehrlich, W. Full, FCM: the fuzzy c-means clustering algorithm, *Comput. Geosci.* 10 (2–3) (1984) 191–203.
- [5] M. Belkin, P. Niyogi, V. Sindhwani, Manifold regularization: a geometric framework for learning from labeled and unlabeled examples, *J. Mach. Learn. Res.* 7 (1) (2016) 2399–2434.
- [6] T. Beyer, M. Weigert, H.H. Quick, U. Pietrzyk, F.M. Vogt, C. Palm, et al., MR-based attenuation correction for torso-PET/MR imaging: pitfalls in mapping MR to CT data, *Eur. J. Nucl. Med. Mol. Imaging* 35 (6) (2008) 1142–1146.
- [7] Y. Berker, J. Franke, A. Salomon, MRI-based attenuation correction for hybrid PET/MRI systems: a 4-class tissue segmentation technique using a combined ultrashort-echo-time/Dixon MRI sequence, *J. Nucl. Med.* 53 (5) (2012) 796–804.
- [8] D. Cusumano, L. Placidi, S. Teodoli, L. Boldrini, L. Azario, On the accuracy of bulk synthetic CT for MR-guided online adaptive radiotherapy, *Radiol. Med.* (2019).
- [9] J. Dickson, C. Omeara, A. Barnes, A comparison of CT- and MR-based attenuation correction in neurological PET, *Eur. J. Nucl. Med. Mol. Imaging* 41 (6) (2014) 1176–1189.
- [10] G. Delso, F. Wiesinger, L.L. Sacolick, Clinical evaluation of zero-echo-time MR imaging for the segmentation of the skull, *J. Nucl. Med.* 56 (3) (2015) 417–422.
- [11] H. Eggers, B. Brendel, A. Duijndam, Dual-echo Dixon imaging with flexible choice of echo times, *Magn. Reson. Med.* 65 (1) (2011) 96–107.
- [12] J.M. Edmund, T. Nyholm, A review of substitute CT generation for MRI-only radiation therapy, *Radiat. Oncol.* 12 (1) (2017) 28.
- [13] B.G. Fallone, B. Murray, S. Rathee, T. Stanescu, S. Steciw, S. Vidakovic, D. Tymofichuk, First MR images obtained during megavoltage photon irradiation from a prototype integrated linac-MR system, *Med. Phys.* 36 (6) (2009) 2084–2088.
- [14] R. Farjam, N. Tyagi, J.O. Deasy, Dosimetric evaluation of an atlas-based synthetic CT generation approach for MR-only radiotherapy of pelvis anatomy, *J. Appl. Clin. Med. Phys.* 20 (1) (2019) 101–109.
- [15] M. Hofmann, F. Steinke, V. Scheel, MR-based attenuation correction for PET/MR: a novel approach combining pattern recognition and atlas registration, *J. Nucl. Med.* 49 (11) (2008) 1875–1883.
- [16] M. Hofmann, B. Pichler, B. Schölkopf, T. Beyer, Towards quantitative PET/MRI: a review of MR-based attenuation correction techniques, *Eur. J. Nucl. Med. Mol. Imaging* 36 (1 Supplement) (2009) 93–104.
- [17] S.H. Hsu, Y. Cao, K. Huang, M. Feng, J.M. Balter, Investigation of a method for generating synthetic CT models from MRI scans of the head and neck for radiation therapy, *Phys. Med. Biol.* 58 (23) (2013) 8419–8435.
- [18] X. Han, MR-based synthetic CT generation using a deep convolutional neural network method, *Med. Phys.* 44 (4) (2017) 1408–1419.
- [19] Y. Huang, S. Member, L. Shao, S. Member, Cross-modality image synthesis via weakly-coupled and geometry co-regularized joint dictionary learning, in: *IEEE Transactions on Medical Imaging*, PP(99), 2017, p. 1–1.
- [20] HU, L., Shao, L., Muzic, R.F., SU, K.-H. and Qian, P., 2017. Systems and methods for translation of medical imaging using machine learning. U.S. Patent App., 15/533457, 2017.
- [21] J. Hong, H. Cheng, Y. Zhang, J. Liu, Detecting cerebral microbleeds with transfer learning, *Mach. Vision Appl.* (2019) 1123–1133.
- [22] G. Janssens, L. Jacques, J.O. De Xivry, X. Geets, B. Macq, Diffeomorphic registration of images with variable contrast enhancement, *Int. J. Biomed. Imaging* (2011) 1–16 ID 891585.
- [23] A. Johansson, M. Karlsson, J. Yu, T. Askund, T. Nyholm, Voxel-wise uncertainty in CT substitute derived from MRI, *Med. Phys.* 39 (6) (2012) 3283–3290.
- [24] E.R. Kops, H. Herzog, Template Based Attenuation Correction for PET in MR-PET Scanners, in: *IEEE Nuclear Science Symposium Conference Record*, 2008, pp. 3786–3789.
- [25] S.M. Lavalley, M.S. Branicky, S.R. Lindemann, On the Relationship between Classical Grid Search and Probabilistic Roadmaps, *Int. Workshop Algorithm. Found. Rob.* (2004) 59–75.
- [26] L. Liu, Y. Cao, J.A. Fessler, S. Jolly, J.M. Balter, A female pelvic bone shape model for air/bone separation in support of synthetic CT generation for radiation therapy, *Phys. Med. Biol.* 61 (1) (2016) 169–182.
- [27] F. Liu, H. Jang, R. Kijowski, T. Bradshaw, A.B. Mcmillan, Deep learning MR imaging-based attenuation correction for PET/MR imaging, *Radiology* (2017) 170700.
- [28] A.L. Leynes, J. Yang, F. Wiesinger, S.S. Kaushik, D.D. Shanbhag, Y. Seo, T.A. Hope, P.E.Z. Larson, Zero-echo-time and Dixon deep pseudo-CT (ZeDD CT): direct generation of pseudo-CT images for pelvic PET/MRI attenuation correction using deep convolutional neural networks with multiparametric MRI, *J. Nucl. Med.* 59 (5) (2017) 852–858.
- [29] A. Martinezmoller, M. Souvatzoglou, G. Delso, R.A. Bundschuh, C. Chefdhotel, S. Ziegler, et al., Tissue Classification as a Potential Approach for Attenuation Correction in Whole-Body PET/MRI: evaluation with PET/CT Data, *J. Nucl. Med.* 50 (4) (2009) 520–526.
- [30] P. Niyogi, Manifold regularization and semi-supervised learning: some theoretical analyses, *J. Mach. Learn. Res.* 14 (1) (2013) 1229–1250.
- [31] D.R. Nayak, Y. Zhang, D.S. Das, S. Panda, MJaya-ELM: a Jaya algorithm with mutation and extreme learning machine based approach for sensorineural hearing loss detection, *Appl. Soft Comput.* (2019).
- [32] P. Qian, Y. Jiang, Z. Deng, L. Hu, R.F. Muzic, Cluster prototypes and fuzzy memberships jointly leveraged cross-domain maximum entropy clustering, *IEEE Trans. Cybern.* 46 (1) (2016) 181–193.
- [33] P. Qian, S. Sun, Y. Jiang, K. Su, T. Ni, S. Wang, R.F. Muzic, Cross-domain, soft-partition clustering with diversity measure and knowledge reference, *Pattern Recognit.* (2016) 155–177.
- [34] P. Qian, K. Zhao, Y. Jiang, K. Su, Z. Deng, S. Wang, R.F. Muzic, Knowledge-Leveraged Transfer Fuzzy C-Means for Texture Image Segmentation with Self-Adaptive Cluster Prototype Matching, *Knowl. Based Syst.* (2017) 33–50.
- [35] P. Qian, J. Zhou, Y. Jiang, F. Liang, K. Zhao, S. Wang, K. Su, R.F. Muzic, Multi-View Maximum Entropy Clustering by Jointly Leveraging Inter-View Collaborations and Intra-View-Weighted Attributes, *IEEE Access* (2018) 28594–28610.
- [36] P. Qian, Y. Chen, J. Kuo, Y. Zhang, Y. Jiang, K. Zhao, R.A. Helo, H. Friel, A. Baydoun, F. Zhou, J. Heo, N. Avriil, K. Herrmann, R. Ellis, B. Traugher, R.S. Jones, S. Wang, K. Su, R.F. Muzic, mDixon-Based Synthetic CT Generation for PET Attenuation Correction on Abdomen and Pelvis Jointly Using Transfer Fuzzy Clustering and Active Learning-Based Classification, *IEEE Trans. Med. Imaging* (2019) 1–1.
- [37] F. Selvaggi, A. Cuocolo, G. Sciaudone, S. Maurea, A. Giuliani, C. Mainolfi, FGD-PET in the follow-up of recurrent colorectal cancer, *Colorect. Dis.* 5 (5) (2003) 496–500.
- [38] W. Schneider, T. Bortfeld, W. Schlegel, Correlation between CT numbers and tissue parameters needed for Monte Carlo simulations of clinical dose distributions, *Phys. Med. Biol.* 45 (2) (2000) 459–478.
- [39] C. Schuld, I. Laptev, B. Caputo, Recognizing human actions: a local SVM approach, in: *Proceedings of the 17th International Conference on Pattern Recognition*, 2004. ICPR, IEEE, 2004, p. 2004.
- [40] A.P. Shah, D.W. Jokisch, D.A. Rajon, C.J. Watchman, P.W. Patton, W.E. Bolch, Chord-based versus voxel-based methods of electron transport in the skeletal tissues, *Med. Phys.* 32 (10) (2005) 3151.
- [41] T. Stanescu, K. Wachowicz, D.A. Jaffray, Characterization of tissue magnetic susceptibility-induced distortions for MRIgRT, *Med. Phys.* 39 (12) (2012) 7185.
- [42] K. Su, L. Hu, C. Stehning, M. Helle, P. Qian, C.L. Thompson, G. Pereira, D.W. Jordan, K.A. Herrmann, M. Traugher, R.F. Muzic, B. Traugher, Generation of brain pseudo-CTs using an undersampled, single-acquisition UTE-mDixon pulse sequence and unsupervised clustering, *Med. Phys.* 42 (8) (2015) 4974–4986.
- [43] T. Sekine, E.E.G.W. Voert, G. Warnock, Clinical evaluation of zero-echo-time attenuation correction for brain 18F-FDG PET/MR: comparison with atlas attenuation correction, *J. Nucl. Med.* 57 (12) (2016) 1927–1932.
- [44] G. Wagenknecht, H.J. Kaiser, F.M. Mottaghy, H. Herzog, MRI for attenuation correction in pet: methods and challenges, *Magn. Reson. Mater. Phys. Biol. Med.* 26 (1) (2013) 99–113.
- [45] J. Wen, Y. Tian, S. Yehang, Improved evidential fuzzy c-means method, *J. Syst. Eng. Electron.* 29 (1) (2018) 187–195.
- [46] D. Wu, J.M. Mendel, Patch Learning, *IEEE Trans. Fuzzy Syst.* (2019) 1906.00158.
- [47] S. Wang, Y. Zhang, M. Yang, B. Liu, J. Ramirez, J.M. Gorriz, Unilateral sensorineural hearing loss identification based on double-density dual-tree complex wavelet transform and multinomial logistic regression, *Integr. Comput. Aided Eng.* 26 (4) (2019) 411–426.
- [48] L. Yang, M. Wang, S. Yang, R. Zhang, P. Zhang, Sparse Spatio-Spectral LapSVM With Semisupervised Kernel Propagation for Hyperspectral Image Classification, *IEEE J. Select. Topics Appl. Earth Observ. Remote Sensing* 10 (5) (2017) 2046–2054.
- [49] H. Zaidi, A. Alavi, Current trends in PET and combined (PET/CT and PET/MR) systems design, *PET Clin.* 2 (2) (2007) 109–123.
- [50] H. Zaidi, O. Mawlawi, C.G. Orton, Simultaneous PET/MR will replace PET/CT as the molecular multimodality imaging platform of choice, *Med. Phys.* 34 (5) (2007) 1525–1528.
- [51] J. Zheng, J. Cao, Z. Wang, F. Liu, S. Wang, T. Wu, Y. Chen, K. Zhao, Y. Jiang, P. Qian, Semi-Automatic Synthetic Computed Tomography Generation for Abdomens Using Transfer Learning and Semi-Supervised Classification, *J. Med. Imaging Health Inform.* 9 (9) (2019) 1878–1886.
- [52] Y. Zhang, V.V. Govindaraj, C. Tang, W. Zhu, J. Sun, High Performance Multiple Sclerosis Classification by Data Augmentation and AlexNet Transfer Learning Model, *J. Med. Imaging Health Inform.* 9 (9) (2019) 2012–2021.